A two–variable model of somatic–dendritic interactions in a bursting neuron

Carlo R. Laing and André Longtin
Department of Physics, University of Ottawa, 150 Louis Pasteur, Ottawa, ON, Canada K1N 6N5.

Submitted to Bulletin of Mathematical Biology
January 22, 2002

Running title: Model of a bursting neuron.

Corresponding author:
Carlo R. Laing
Department of Physics,
University of Ottawa,
150 Louis Pasteur,
Ottawa, ON,
Canada K1N 6N5.

ph: (613) 562 5800 extn 6744
fax: (613) 562 5190
email: claing@science.uottawa.ca

We would like to submit the final manuscript electronically in LaTeX format.

A two–variable model of somatic–dendritic interactions in a bursting neuron

Abstract

We present a two–variable delay–differential–equation model of a pyramidal cell from the electrosensory lateral line lobe of a weakly electric fish that is capable of burst discharge. It is a simplification of a 6-dimensional ordinary differential equation model for such a cell whose bifurcation structure has been analyzed (Doiron et al., J. Comput. Neurosci., to appear). We have modeled the effects of back–propagating action potentials by a delay, and use an integrate–and–fire mechanism for action potential generation. The simplicity of the model presented here allows one to explicitly derive a two–dimensional map for successive interspike intervals, and to analytically investigate the effects of time–dependent forcing on such a model neuron. Some of the effects discussed include "burst excitability", the creation of resonance tongues under periodic forcing, and stochastic resonance.

1 Introduction

Bursting, in which a cell periodically switches from quiescent behavior to a rapidly spiking state and back again, is an important and common form of behavior [17, 19, 24, 25, 31, 38]. A number of mathematical models of bursting cells have been developed [5, 31, 38, 39], but they are generally difficult to treat analytically in any detail. Much past analysis of bursting cells has been influenced by the "slow–fast" separation of timescales in bursting systems [17, 31], where it is assumed that fast, spiking variables act on a much shorter timescale than the slow variable(s) that are responsible for the shifts between spiking and quiescent behavior.

Recently, a new mechanism for burst discharge in pyramidal cells of the weakly electric fish *Apteronotus leptorhyncus* was investigated [5]. These cells receive input directly from electroreceptor cells on the fish's skin, and are thought to play a significant role in the processing of electrosensory information. The model presented in [5] was a set of six coupled nonlinear first–order ordinary differential equations, which was a reduction from the multicompartment model involving over 1500 variables presented in [6]. This reduction was obtained by lumping the many compartments into two, representing the soma and the dendrite, and by ignoring the dynamics of the channels not thought to be important in the mechanism for bursting. That the model in [5] reproduced both the bursting behavior observed in the model of [6] and experimentally observed bursts [24] indicates that this process was successful.

The model analyzed in [5] was studied using the "slow–fast" approach of others [17, 31], but it differed from all previous bursting models in that it had only one slow variable; when that variable was held constant, the remaining "fast" system did not show bistability. The bifurcation in the fast system that ended a burst was found to be a transition from period–one to period–two behavior associated with the failure of a somatic action potential to induce a dendritic one, and the interburst interval was found to involve the passage in phase space near a fixed point. Several aspects of the timing of bursts were found to be related to the distance in parameter space from a saddle–node bifurcation, hence the name "ghostbursting" [35].

In this paper we further reduce the model in [5] to a set of two discontinuous delay differential equations, from which a two–dimensional map can be derived (assuming constant input current). This gives us analytical insight into complex soma–dendrite interactions. This reduced model can be constructed because, as a result of the work in [5], we understand the essential ingredients of this type of bursting (refer to Figure 1). A short time after most somatic spikes, current flows from the dendrite to the soma, producing a depolarizing afterpotential (DAP) at the soma. For large enough current injected to the soma, the sizes of these DAPs slowly increase due to a slow inactivation of the dendritic potassium that is responsible for the repolarization of dendritic action potentials. This results in progressively smaller inter–spike intervals (ISIs), and this process continues until an ISI is smaller than the refractory period of the dendrite. Once this happens, there is dendritic spike failure, which removes the normal current flow to the soma, and a DAP does not appear. This results in a long ISI, during which the variable controlling inactivation of dendritic potassium increases, and the sequence starts again. In Figure 1 we show typical bursting behavior from the model in [5]. The spike patterning is similar to that seen in the multicompartment model in [6] and in experimental recordings [24].

If we consider gradually increasing the DC current injected into the soma of such an actual pyramidal cell, it is observed that the cell's behavior changes from quiescent to periodic firing and then to bursting [7, 24], and this behavior is seen in the pyramidal cell models [5, 6]. The model presented below also shows these transitions.

In this paper we also consider periodically modulating the current applied to the model neuron, and for the case of sinusoidal modulation we obtain a three–dimensional map for successive spike times. This map can be used to determine the boundaries in parameter space of resonance tongues, in which the neuron's firing frequency is locked to that of the forcing. This map is able to explain some of the behavior seen in [23], e.g. that sinusoidal modulation of the applied current about a DC level can either increase or decrease the value of this DC current where the neuron changes from periodic to bursting behavior, depending on the frequency of forcing. The simplified model presented here can also reproduce the phenomenon of "burst excitability" that is explored in more detail in [22], and by varying parameters, the "gallery" of burst types seen in [5].

The two–dimensional model that we have developed would be very useful for large–scale simulations of networks of such neurons as it has fewer variables than common neuron models that involve ionic channels [5], the differential equations involved are not stiff, and its piecewise linear nature aids its analysis. The way we have modeled backpropagation of an action potential along a dendrite and the resulting "ping–pong" effect [40] by a discrete delay in a low–dimensional system is also novel. This type of modeling could possibly be applied to other systems in which backpropagation in active dendrites (or more generally, having different voltages in different parts of a cell at the same time) is thought to be important [9, 16, 20, 26, 28, 33].

In Section 2 we present the model, derive the corresponding map and investigate its properties. In Section 3 we present the sinusoidally forced model, derive the corresponding map, and discuss resonance tongues and stochastic resonance. Section 4 is a summary and discussion. The appendix contains a discussion of other possible models that show "ghostbursting".

2 The Model

We use an integrate–and–fire neuron [18] to produce action potentials ("spikes"), and couple this with another variable, c, whose behavior mimics the effects of inactivation of dendritic potassium in the model of [5] (although c increases during a burst, while the actual inactivation gating variable decreases in [5] (see Figure 1); both trends have the same effect in their respective models). The effective delay between a somatic spike and the appearance of a DAP (a result of the diffusive coupling in voltage between soma and dendrite in [5]) is mimicked by an actual delay, and the effect of the DAP is mimicked by an instantaneous increase in the neuron's voltage.

The equations are

$$\frac{dV}{dt} = I - V + Ac\sum_n H(t_n - t_{n-1} - r)\delta(t - t_n - \sigma) \quad (1)$$

$$\frac{dc}{dt} = -c/\tau + (B + Cc^2)\sum_n \delta(t - t_n) \quad (2)$$

with the rule $V(t_n^+) = 0$ if $V(t_n^-) = 1$, and the t_n are the times at which the reset occurs (n is an integer). V is voltage, I is injected current, $H(\cdot)$ is the Heaviside function, r represents the refractory period of the dendrite, σ is the effective delay between the somatic action potential and the dendritic–to–somatic current that causes the DAP, and A, B, C and τ are constants. The action potentials are thought of as occurring at the times t_n.

At almost all times, V exponentially approaches I from below with time–constant 1, and c exponentially decays towards 0 with time–constant τ. At each firing time t_n, c is incremented: $c \mapsto c + B + Cc^2$. At a time σ after firing, and assuming that the previous ISI, $t_n - t_{n-1}$, is greater than the refractory period r, V is incremented: $V \mapsto V + Ac$, where c is evaluated at a time σ after firing. If the previous ISI is less than the refractory period, V is not incremented. Note that the neuron will not fire if I is always less than 1.

An example of the behavior of (1)-(2) is shown in Figure 2. Note the increase in the overall level of c and the decrease of ISIs during the burst, and the long ISI separating bursts. This long ISI is a result of the previous ISI being less than the refractory period of the dendrite of the neuron, so that no current propagates from the dendrite to the soma during this ISI. This long ISI can also be seen as the smallest instantaneous frequency in Figure 3 for I greater than ~ 1.22. This bursting behavior is quite robust with respect to changes in parameters.

We now derive an exact map describing the behavior of (1)-(2).

2.1 Derivation of the map

Because of the linearity of (1)-(2) for values of t at which the δ functions are zero, it is possible to derive a map for interspike intervals and values of c just after firing. Recall that the solution of (1) when $A = 0$ is

$$V(t) = I + [V(0) - I]e^{-t} \tag{3}$$

Assume that $t = t_n^+$, $V(t_n^+) = 0$, $c(t_n^+) = c_n$, and $t_n - t_{n-1} > r$. ($V(t_n^+)$ is defined as $\lim_{\varepsilon \to 0} V(t_n + \varepsilon)$, where $\varepsilon > 0$.) At a time σ after t_n^+, when $V = I(1 - e^{-\sigma})$ and $c = c_n e^{-\sigma/\tau}$, V is incremented by $Ac_n e^{-\sigma/\tau}$. Assuming that this does not push V above 1, i.e. that $I(1 - e^{-\sigma}) + Ac_n e^{-\sigma/\tau} < 1$, V continues to evolve, reaching 1 after a further time s, where

$$I + [I(1 - e^{-\sigma}) + Ac_n e^{-\sigma/\tau} - I]e^{-s} = 1 \tag{4}$$

($s = 0$ when $t = t_n + \sigma$). Solving (4) for s we obtain

$$s = \ln\left(\frac{Ac_n e^{-\sigma/\tau} - Ie^{-\sigma}}{1 - I}\right) \tag{5}$$

Alternatively, if $t_n - t_{n-1} < r$ (i.e. the last ISI was less than the refractory period of the dendrite, so there is no feedback from dendrite to soma), V will reach 1 after a time

$$\ln\left(\frac{I}{I-1}\right), \tag{6}$$

measured from t_n. During the interval (t_n, t_{n+1}), c exponentially decays with time constant τ, and is then updated at time t_{n+1}. Thus we have a piecewise two–dimensional map for $\Delta_{n+1} \equiv t_{n+1} - t_n$ and c_{n+1} in terms of Δ_n and c_n:

$$\Delta_{n+1} = \begin{cases} \sigma & \text{if } \Delta_n > r \text{ and } I(1 - e^{-\sigma}) + Ac_n e^{-\sigma/\tau} > 1 \quad (i) \\ \sigma + \ln\left(\frac{Ac_n e^{-\sigma/\tau} - Ie^{-\sigma}}{1-I}\right) & \text{if } \Delta_n > r \text{ and } I(1 - e^{-\sigma}) + Ac_n e^{-\sigma/\tau} < 1 \quad (ii) \\ \ln\left(\frac{I}{I-1}\right) & \text{if } \Delta_n < r \quad (iii) \end{cases} \tag{7}$$

$$c_{n+1} = c_n e^{-\Delta_{n+1}/\tau} + B + C[c_n e^{-\Delta_{n+1}/\tau}]^2 \tag{8}$$

This is all under the assumption that $I(1 - e^{-\sigma}) < 1$, i.e. that neither I nor σ are too large. If this inequality is not satisfied, e.g. if I is too large, then $\Delta_{n+1} = \ln[I/(I-1)]$ as in case (*iii*) above. As can be seen from (8), the small value of Δ_{n+1} in this situation may cause the values of c_i to increase without bound.

The instantaneous frequency, i.e. $1/\Delta_n$, is shown as a function of I in Figure 3 for a particular set of parameter values (transients have been removed). A number of observations can be made:

1. During periodic firing for $1 < I <\sim 1.22$, case (*ii*) in (7) will always be true. For periodic firing, $c_{n+1} = c_n$, and thus (8) is a quadratic in c_n. It can therefore be solved for c_n in terms of the steady–state period, Δ (the negative square root must be chosen). Substituting this into case (*ii*) in (7), we obtain an equation that Δ must satisfy:

$$(1 - I)e^{-\sigma}e^{\Delta} = \frac{Ae^{-\sigma/\tau}\left[1 - e^{-\Delta/\tau} - \sqrt{1 - 2e^{-\Delta/\tau} + (1 - 4BC)e^{-2\Delta/\tau}}\right]}{2Ce^{-2\Delta/\tau}} - Ie^{-\sigma} \tag{9}$$

For $1 < I <\sim 1.22$, equation (9) has two solutions, the larger one of which is stable. The two solutions coalesce in a saddle–node bifurcation [21] at $I \sim 1.22$. Note that in (1)-(2), this is a saddle–node bifurcation of periodic orbits. Interestingly, this was the bifurcation separating periodic from bursting behavior in the full ionic ODE model in [5]. As $I \to 1$ from above, the largest root of (9) tends to ∞, corresponding to the frequency tending to zero. Note that if $\tau = 1$, (9) is independent of σ.

2. For I greater than ~ 1.22, the smallest instantaneous frequency occurs between bursts, where the only current driving the neuron during its entire period is I. Thus the lower curve in Figure 3 for I greater than ~ 1.22 is just $\Delta = \ln [I/(I-1)]$ (case (*iii*) in (7)).

3. For I greater than ~ 1.22, the "band" of frequencies in Figure 3 not including the interburst interval is bounded below by the curve

$$\Delta = \sigma + \ln \left(\frac{ABe^{-\sigma/\tau} - Ie^{-\sigma}}{1-I} \right) \tag{10}$$

since c_n has a minimum value of B after being reset at the end of the inter–burst interval. (Expression (10) is obtained by setting $c_n = B$ in (7) (*ii*)).

4. For I greater than ~ 1.45, the map alternates between cases (*i*) and (*iii*) in (7), so only the longest Δ_n is a function of I.

5. The progression quiescence $\to$ periodic firing $\to$ bursting $\to$ alternating short and long ISIs as I is increased as seen in Figure 3 is also seen in the models of [5, 6], and experimental recordings [24, 37].

In relation to point 1 above, if the positive square root is taken instead and substituted into case (*ii*) in (7), the roots of the resulting function may not satisfy the condition $\Delta > r$ associated with case (*ii*), and thus they will not be actual fixed points of the map. Also, the fact that (8) can be solved explicitly for the steady state value of c is a result of our choice of the dynamics of c, (2). Replacing the term Cc^2 in (2) by Cc would mean that the equation for the steady state of c was linear and thus had only one solution; this choice would also simplify the expression (9), but would make chaotic behavior more difficult, although not impossible, to obtain (see below).

2.2 Lyapunov exponent

The Lyapunov exponents of a trajectory determine its stability and the behavior of nearby trajectories. If a stable solution has at least one positive Lyapunov exponent, the system will exhibit sensitivity to initial conditions, and nearby trajectories will typically separate exponentially in time. For a range of current values, the bursting behavior in [5] was shown to have a positive Lyapunov exponent, and thus be chaotic.

To find the maximal Lyapunov exponent, λ, for a trajectory of the map (7)-(8), we analytically calculate the Jacobian, Df, of (7)-(8), evaluate it at each point on the orbit, $x_1, x_2, \ldots$, where $x_i = (\Delta_i, c_i) \in \mathbf{R}^2$ and form the vectors

$$k_n = Df(x_n)k_{n-1} \tag{11}$$

where k_0 is a randomly chosen initial vector in $\mathbf{R}^2$. The k_n will quickly line up with the direction of greatest expansion, and λ can be calculated from

$$\lambda = \lim_{n\to\infty} \frac{\ln |k_n|}{n} \tag{12}$$

This quantity is shown in Figure 4, multiplied by 4 for clarity, together with instantaneous frequency. Note the transition from period–1 firing to chaotic bursting at $I \sim 1.22$, and the long–period quasiperiodic behavior for I greater than ~ 1.32.

In Figure 5 we show the norm of k_n as a function of n, together with c_n. Note that the k_n actually shrink during the first part of a burst, but grow towards the end of it, where the Cc^2 term in (2) becomes significant. For the parameters in Figure 5, the k_n grow exponentially in time, leading to a positive Lyapunov exponent.

2.3 Effects of parameters

The model (1)-(2) has six parameters that are regarded as constant (A, r, σ, τ, B and C). We now briefly discuss the effects of changing each of these.

- A mimics the size of the current flowing from dendrite to soma, and thus the size of the DAP and how much it contributes towards moving the soma to spike threshold. Thus increasing A will make the neuron more likely to burst.

- r is irrelevant during periodic firing (note that (9) is independent of r), so changing it cannot switch the neuron from periodic to bursting or vice versa. However, decreasing r makes the bursting more likely to be chaotic. This is because c can now reach a larger value at the end of a burst before it is terminated, and it is the nonlinear growth of c at the end of the burst that is the source of the chaos (see Figure 5). However, if c can take on large values at the end of a burst, there may not be time during the interburst interval for c to decay sufficiently before the beginning of the next burst, and this can lead to a "blow–up" in c. Note that r must be greater than σ.

- τ governs the rate of decay of c. Whether the neuron fires periodically or bursts depends on the balance between the decay of c between spikes and the increment in c at each spike. As seen from (8), increasing τ causes c to decay more slowly, making the neuron more likely to burst. Note from (1)-(2) that the time–constants governing the dynamics of V and c are 1 and τ respectively, and that it is possible for bursting to occur with $\tau < 1$ (not shown). This is in contrast to the usual analysis of bursting, where there is assumed to be a separation between the fast spiking dynamics and the slower dynamics that control the burst length and interburst intervals [17, 31].

  Also, as in [5], there is a range of τ values for which bursting is seen as I is varied. If τ is too small, c decays too much between action potentials, and the slow growth during a burst does not occur. Similarly, if τ is too large, c cannot decay between bursts and the successive maxima of c grow extremely quickly. This leads to "doublet" firing in V and an eventual breakdown of the algorithm.

- For the parameters used, if $\tau > 1$, increasing σ makes the neuron more likely to burst and vice versa. If $\tau < 1$, increasing σ makes the neuron less likely to burst, and vice versa. This can be understood graphically by writing (9) as

$$e^{-\sigma} f(\Delta) = A e^{-\sigma/\tau} g(\Delta, \tau) \tag{13}$$

  where

$$f(\Delta) = I + (1 - I)e^{\Delta} \quad \text{and} \quad g(\Delta, \tau) = \frac{1 - e^{-\Delta/\tau} - \sqrt{1 - 2e^{-\Delta/\tau} + (1 - 4BC)e^{-2\Delta/\tau}}}{2Ce^{-2\Delta/\tau}} \tag{14}$$

  For a given τ and other parameters in the appropriate range, $f(\Delta)$ is a concave–down function of Δ, and $g(\Delta, \tau)$ is a concave–up function of Δ. They are both positive in the region of interest. The intersections of the left and right sides of (13) give the values of Δ at the two periodic orbits (one stable and the other unstable) of (1)-(2). It is the coalescence of these in a saddle–node bifurcation that marks the transition from periodic to bursting behavior.

  If $\tau > 1$, increasing σ decreases the left hand side of (13) more than it decreases the right hand side, bringing the two points of intersection closer to one another, and thus lowering the value of I at which the saddle–node bifurcation occurs. Conversely, if $\tau < 1$, increasing σ decreases the right hand side of (13) more than it decreases the left hand side, moving the two points of intersection further apart and thus increasing the value of I at which the saddle–node bifurcation occurs.

- B and C both control the increment in c at each spike, so increasing either will make the neuron more likely to burst. The Cc^2 term is not strictly necessary to obtain bursts, as we can produce a plot like Figure 3 with $C = 0$ (although the bursts are then periodic, not chaotic). However, without this nonlinear term it is difficult to obtain chaotic bursts. This is because it is the nonlinear growth of c at the end of a burst, and the fact that the largest value of c during a burst is carried over to the start of the next burst, that cause chaotic dynamics to occur (see Figure 5). If $B = 0$ then $c_n = 0$ for all n is a possible solution of (8), and having a nonzero value of B prevents this.

This knowledge is useful, since if we can determine the qualitative relationship between parameters in a more realistic model of this cell (e.g. the models in [5, 6]) and the six parameters above, we can understand how changing the parameters in the more realistic models will change the behavior of the cell, without having to simulate those more detailed models.

2.4 Burst excitability

The presence of a saddle–node bifurcation of fixed points of the map (7)-(8) marking the transition between periodic and burst behavior implies "burst excitability" at this boundary, as was discussed in [22]. For a value of I less than that at the bifurcation, a transient increase in I may induce a burst in which the firing rate is elevated from its prior value for a time greater than the duration of the increase in I. If the magnitude of the increase in I is not sufficient, or its duration is too short, a burst will not be observed. Such behavior is shown in Figure 6. Note that the length of the burst in Figure 6, top, (i.e. the time between the perturbation of I and the doublet marking the end of the burst) is about four times the length of the longest time constant in the system ($\tau = 1$). The recovery from the perturbation in Figure 6, bottom, is even longer. This reinforces the idea presented in [5] that "slow" behavior in a bursting system does not necessarily imply the existence of a slow time–scale in the form of an explicit long time–constant.

2.5 A "gallery" of bursts

We know for the system (1)-(2) that the current threshold for spiking is $I = 1$, and that the length of an interburst interval is given by $\Delta = \ln[I/(I-1)]$, which tends to infinity as I tends to 1 from above. Also, since the bifurcation separating periodic from bursting behavior is a saddle-node bifurcation of periodic orbits, standard results regarding type–I intermittency [29] show that the number of spikes in a burst scales as

$$N \sim \frac{1}{\sqrt{I - I_{sn}}} \tag{15}$$

as I tends to I_{sn} from above, where I_{sn} is the value of I at which the saddle–node bifurcation occurs (~ 1.22 in Figure 3). I_{sn} is a function of the other parameters in the system, but if we can change them so that I_{sn} moves relative to the spiking threshold of 1 (and in particular, if we can make it approach 1), then we will be able to obtain a wide variety of different burst lengths and interburst intervals, as was done in [5].

In Figure 7 we show such a situation, where we have chosen to vary B. We can see that the curve separating periodic from burst firing touches the curve separating quiescence from periodic firing (the line $I = 1$) near $B = 0.42$. This is similar to the situation in [5], where the maximum conductance of dendritic potassium was varied. Note that the curve in this Figure can be found numerically from (9) by determining the value of I as a function of B at which the two roots of (9) coalesce; the map, (7)-(8), does not have to be iterated.

By choosing different points in Figure 7 we can obtain different bursts — this is shown in Figure 8. In the top panel, we are close to the curve of saddle–node bifurcations of periodic orbits, but far from $I = 1$. Hence the bursts are long (compare with those in Figure 2) but the interburst interval is not particularly so. In the middle panel, we are close to the codimension–two point in Figure 7 (marked with a circle), so both the bursts and the interburst intervals are long. In the bottom panel we are to the right of the codimension–two point in Figure 7, and (as was observed in [5]) we observe doublets, i.e. a small ISI followed by a larger one. This is easily understood, since the first spike induces a large DAP (large because B is large) which induces a second spike. This second one marks the end of an ISI that is within the refractory period of the dendrite, so no DAP arrives after it and a long ISI is produced (long because I is close to 1).

One difference between the model (1)-(2) and the ODE model of [5] involves the scaling of the interburst intervals as I decreases. The bifurcation separating quiescence from periodic firing in [5] is a saddle–node–on–a–circle bifurcation [21], and hence the period of periodic firing scales as $T \sim 1/\sqrt{I - I^*}$, where I^* is the value of the current at which the transition takes place. This is in contrast with the $\Delta = \ln[I/(I-1)]$ expression for the integrate–and–fire mechanism that we are using in (1)-(2) to produce action potentials. Thus in the interburst intervals, where there is essentially no current flowing from the dendrite to the soma and the soma is driven by only the current injected into it from the outside, the length of the interburst intervals will scale differently with current for the two models. However, both scalings give the same qualitative result, i.e. $T \to \infty$ as $I \to I^*$ from above, and $\Delta \to \infty$ as $I \to 1$ from above. The scaling in (1)-(2) could be made to match the scaling in [5] if the spike–producing neuron was one whose bifurcation separating quiescence from periodic firing was a saddle–node–on–a–circle bifurcation; one example is the "theta neuron" [15], but its nonlinearity would complicate analysis of the resulting bursting model.

3 Sinusoidal forcing

The response of dynamical systems to periodic forcing is a widely studied problem. Examples with biological motivation include [3, 4, 11, 12, 14, 18, 34]. We will now consider the situation where I in (1) is sinusoidally modulated. The modulation has amplitude Γ and angular frequency ω. This form of forcing is relevant for the following reasons. Wave–type weakly electric fish, e.g. *Apteronotus leptorhyncus*, continuously generate an approximately sinusoidal modulation of the electric field surrounding them via their electric organ discharge (EOD). The frequency of this oscillation can be as high as 1200 Hz and is essentially constant for any particular fish. Males have higher frequencies than females. When two fish are physically close, the difference in EOD frequencies gives rise to a "beat" frequency, equal to the difference between the two EOD frequencies. Thus there are at least two types of sinusoidal inputs (the fish's own EOD and the beating oscillation) that may be detected by electroreceptors on the fish's skin [1, 27] and passed to the pyramidal cells that we are modeling.

We will now derive a map similar to (7)-(8) for the case where I in (1) is sinusoidally modulated. Since the dynamics are no longer invariant with respect to time translation, we find that they can only be reduced to a three–dimensional map, rather than a two–dimensional one as above.

Assume that $t = t_n^+$, $V(t_n^+) = 0$, $c(t_n^+) = c_n$, and that $t_n - t_{n-1} > r$. V evolves under

$$\frac{dV}{dt} = I - V + \Gamma \sin(\omega t) \tag{16}$$

which has the solution

$$\begin{aligned} V(t; t_n) &= I[1 - e^{-(t-t_n)}] + \left(\frac{\Gamma}{1+\omega^2}\right)\{\sin(\omega t) - \omega\cos(\omega t)\} \\ &- \left(\frac{\Gamma e^{-(t-t_n)}}{1+\omega^2}\right)[\sin(\omega t_n) - \omega\cos(\omega t_n)] \end{aligned} \tag{17}$$

Note that this satisfies $V(t_n; t_n) = 0$. At a time σ after t_n,

$$\begin{aligned} V = \overline{V} &\equiv I(1 - e^{-\sigma}) + \left(\frac{\Gamma}{1+\omega^2}\right)\{\sin[\omega(t_n+\sigma)] - \omega\cos[\omega(t_n+\sigma)]\} \\ &- \left(\frac{\Gamma e^{-\sigma}}{1+\omega^2}\right)[\sin(\omega t_n) - \omega\cos(\omega t_n)] \end{aligned} \tag{18}$$

and $c = c_n e^{-\sigma/\tau}$. (We assume that $V(t; t_n) < 1$ for $t_n < t \le t_n + \sigma$.) $\overline{V}$ is now incremented by an amount $Ac_n e^{-\sigma/\tau}$. If $\overline{V} + Ac_n e^{-\sigma/\tau} > 1$, i.e. if this increment pushes V over the threshold for firing, then $t_{n+1} = t_n + \sigma$. If this is not the case, we need to solve (16) with $V(t_n + \sigma) = \overline{V} + Ac_n e^{-\sigma/\tau}$. This has the solution

$$\begin{aligned} V(t; t_n, c_n) &= I + \left(\frac{\Gamma}{1+\omega^2}\right)[\sin(\omega t) - \omega\cos(\omega t)] \\ &\quad + e^{-(t-t_n-\sigma)}\left[\overline{V} + Ac_n e^{-\sigma/\tau} - I - \left(\frac{\Gamma}{1+\omega^2}\right)\{\sin[\omega(t_n+\sigma)] - \omega\cos[\omega(t_n+\sigma)]\}\right] \qquad (19) \\ &= I + \left(\frac{\Gamma}{1+\omega^2}\right)[\sin(\omega t) - \omega\cos(\omega t)] \\ &\quad + e^{-(t-t_n-\sigma)}\left[Ac_n e^{-\sigma/\tau} - Ie^{-\sigma} - \left(\frac{\Gamma e^{-\sigma}}{1+\omega^2}\right)[\sin(\omega t_n) - \omega\cos(\omega t_n)]\right] \qquad (20) \end{aligned}$$

and t_{n+1} is the smallest solution greater than t_n of

$$V(t_{n+1}; t_n, c_n) = 1 \qquad (21)$$

All of the above is under the assumption that $t_n - t_{n-1} > r$. If $t_n - t_{n-1} < r$, then from (17), t_{n+1} is the smallest solution (greater than t_n) of

$$\begin{aligned} 1 &= I\left[1 - e^{-(t_{n+1}-t_n)}\right] + \left(\frac{\Gamma}{1+\omega^2}\right)[\sin(\omega t_{n+1}) - \omega\cos(\omega t_{n+1})] \\ &\quad - \left(\frac{\Gamma e^{-(t_{n+1}-t_n)}}{1+\omega^2}\right)[\sin(\omega t_n) - \omega\cos(\omega t_n)] \qquad (22) \end{aligned}$$

During the time interval (t_n, t_{n+1}), c decays exponentially with time–constant τ. Thus we have a piecewise map for t_{n+1} and c_{n+1} in terms of t_n, t_{n-1} and c_n:

$$t_{n+1} = \begin{cases} t_n + \sigma & \text{if } t_n - t_{n-1} > r \text{ and } \overline{V} + Ac_n e^{-\sigma/\tau} > 1 \\ \min\{s > t_n : V(s; t_n, c_n) = 1\} & \text{if } t_n - t_{n-1} > r \text{ and } \overline{V} + Ac_n e^{-\sigma/\tau} < 1 \\ \min\{s > t_n : \Lambda(s; t_n) = 1\} & \text{if } t_n - t_{n-1} < r \end{cases} \qquad (23)$$

$$c_{n+1} = c_n e^{-(t_{n+1}-t_n)/\tau} + B + C\left[c_n e^{-(t_{n+1}-t_n)/\tau}\right]^2 \qquad (24)$$

where $\Lambda(s; t_n) = V(s; t_n)$ and $V(s; t_n)$ is given by (17), and $V(s; t_n, c_n)$ is given by (20).

We can write the map (23)-(24) as

$$\begin{aligned} t_{n+1} &= f(t_n, t_{n-1}, c_n) \qquad (25) \\ c_{n+1} &= g(t_{n+1}, t_n, c_n) = g(f(t_n, t_{n-1}, c_n), t_n, c_n) \equiv h(t_n, t_{n-1}, c_n) \qquad (26) \end{aligned}$$

or

$$\begin{aligned} t_{n+1} &= f(t_n, s_n, c_n) \qquad (27) \\ s_{n+1} &= t_n \qquad (28) \\ c_{n+1} &= h(t_n, s_n, c_n) \qquad (29) \end{aligned}$$

i.e. a map from $\mathbf{R}^3$ to $\mathbf{R}^3$, where

$$g(a, b, c) = ce^{-(a-b)/\tau} + B + C\left[ce^{-(a-b)/\tau}\right]^2 \qquad (30)$$

and f is given by (23).

Note that when $\Gamma = 0$, $\min\{s > t_n : V(s; t_n, c_n) = 1\}$ has the solution

$$s = t_n + \sigma + \ln\left(\frac{Ac_n e^{-\sigma/\tau} - Ie^{-\sigma}}{1 - I}\right) \qquad (31)$$

and $\min\{s > t_n : \Lambda(s;t_n) = 1\}$ has the solution $s = t_n + \ln[I/(I-1)]$, and the map (23)-(24) reduces to (7)-(8), which only involves time differences, as is expected from a time–translationally invariant system. The nonzero amplitude of forcing in (16) breaks this invariance. Note also that the maximal Lyapunov exponent for the map (27)-(29) can be calculated in a similar way to that for the two–dimensional map (7)-(8) (see Section 2.2).

3.1 Arnold tongues

Much work has been done on periodically forced oscillators [3, 11, 12, 14], and it is well–known that an oscillator can become entrained to the frequency of the forcing. This may be of relevance for the model we are considering, since (as mentioned above) the pyramidal cells that we are modeling receive direct afferent input from electroreceptors on the fish's skin. This input has periodic components, and if a pyramidal cell was entrained to its inputs, it could faithfully track that frequency over some range. Moving between an entrained state and a bursting state may also be a useful mechanism for signaling some aspect of a changing input.

Regions of parameter space in which the frequency of the forcing and the frequency of the forced oscillator have a particular ratio are called "Arnold tongues" [12], and are labeled by the ratio of frequencies, e.g. $3:2$. (For this example, the oscillator would pass through 2 cycles in the same time that the forcing signal took to pass through 3 cycles.) The system (1)-(2) is capable of periodically oscillating for some values of its parameters and input, so under periodic forcing we expect it to have some features in common with periodically forced oscillators. However, the presence of the bifurcation separating periodic from burst firing in the unforced system may mean that new features appear when it is periodically forced.

Consider the case of $q:1$ locking, where we have 1 firing during a period of qT ($\omega = 2\pi/T$), i.e. during q forcing cycles. For this case, $c_{n+1} = c_n$, so let c^* be the smallest root of

$$c_n = c_n e^{-qT/\tau} + B + C\left[c_n e^{-qT/\tau}\right]^2 \tag{32}$$

We can see from (20) that in this periodically–locked state

$$\begin{aligned} 1 &= I + \left(\frac{\Gamma}{1+\omega^2}\right)[\sin(\omega t_{n+1}) - \omega\cos(\omega t_{n+1})] \\ &+ e^{-(t_{n+1}-t_n-\sigma)}\left[Ac^* e^{-\sigma/\tau} - Ie^{-\sigma} - \left(\frac{\Gamma e^{-\sigma}}{1+\omega^2}\right)[\sin(\omega t_n) - \omega\cos(\omega t_n)]\right] \end{aligned} \tag{33}$$

Noting that for this locked state

$$\sin(\omega t_{n+1}) - \omega\cos(\omega t_{n+1}) = \sin(\omega t_n) - \omega\cos(\omega t_n) \tag{34}$$

and defining the firing phase in the same way as Chacron et al. [2] as

$$\phi_n = \omega\left(t_n - T\mathrm{int}\left[\frac{t_n}{T}\right]\right), \qquad 0 \le \phi_n < 2\pi \tag{35}$$

where $\mathrm{int}[x]$ is the integer part of x, we see that we can rewrite (33) as

$$1 = I + (1 - e^{-qT})\left(\frac{\Gamma}{1+\omega^2}\right)[\sin\phi_n - \omega\cos\phi_n] + e^{-(qT-\sigma)}[Ac^* e^{-\sigma/\tau} - Ie^{-\sigma}] \tag{36}$$

where c^* is the smallest root of (32). Regarding ϕ_n as a variable, equation (36) typically has either zero or two roots, and if it has two, they are destroyed in a saddle–node bifurcation as a parameter is varied. These saddle–node bifurcations mark the edge of the $q:1$ tongue in parameter space, and a $q:1$ orbit can only exist within such a tongue.

Combining the two terms involving ϕ_n, equation (36) can be rewritten as

$$1 - I - e^{\sigma - qT}[Ac^* e^{-\sigma/\tau} - Ie^{-\sigma}] = (1 - e^{-qT})\left(\frac{\Gamma}{\sqrt{1+\omega^2}}\right)\sin(\phi_n - \tan^{-1}\omega) \tag{37}$$

The saddle–node bifurcations occur when

$$\phi_n = \pi/2 + \tan^{-1}\omega \quad \text{or} \quad \phi_n = 3\pi/2 + \tan^{-1}\omega \tag{38}$$

at which point the right hand side of (37) is

$$\frac{\Gamma(1-e^{-qT})}{\sqrt{1+\omega^2}} \quad \text{or} \quad -\frac{\Gamma(1-e^{-qT})}{\sqrt{1+\omega^2}} \tag{39}$$

respectively. Using this and rearranging (37) we see that the two values of I between which $q:1$ orbits exist are

$$I = \frac{1 - Ac^{*}e^{-\sigma/\tau}e^{\sigma - qT}}{1-e^{-qT}} \pm \frac{\Gamma}{\sqrt{1+\omega^2}} \tag{40}$$

As an example, in Figure 9 we show the boundaries of the $1:1$ tongue, calculated using (40). This expression only gives the region in parameter space where such orbits exist, but says nothing about their stability. For ω less than ~ 6.5, there always appears to be an orbit which is stable between the saddle–node bifurcations that mark the edges of the tongues, but for ω greater than ~ 6.5, the $1:1$ orbit can lose stability through a Hopf bifurcation (dashed curve in Figure 9; this curve was determined by numerically finding fixed points of (27)-(29) and evaluating the eigenvalues of a numerically–determined approximation of the Jacobian of (27)-(29) at those points). This bifurcation is subcritical, and one consequence of that is the bistability of the periodically–forced system, at least in some neighborhood to the left of this dashed line. This bistability has also been observed in the periodically forced 6–dimensional model [23]. Note that this procedure for determining the boundaries of the tongues is not affected by the presence of the periodic $\to$ bursting boundary in parameter space. A similar observation was made in [41], where the authors studied a periodically forced Fitzhugh–Nagumo system as the underlying dynamics changed from excitable to oscillatory.

Recall from Figure 4 that when no forcing is applied, the system moves from periodic firing to bursting at $I \approx 1.22$. Thus, periodic forcing can *increase* the value of the DC component of the applied current at which the system moves from periodic firing to bursting, e.g. at $\omega = 6$ in Figure 9, as shown in Figure 10. Sinusoidal modulation can also *decrease* the value of the DC component of the applied current at which the system moves from periodic firing to bursting, e.g. at $\omega = 7.1$, as shown in Figure 11.

This process can be carried out for other frequency ratios, but the resulting equations are more complicated.

3.2 Stochastic Resonance

Stochastic resonance is the phenomenon whereby moderate amounts of noise, when added to a system that has a subthreshold input signal, cause the signal to be observable in the system's output [10]. For small noise intensities the signal cannot be observed, as it is subthreshold, and for high intensities the system's output is swamped by the noise, so if the signal to noise ratio at the output is plotted as a function of noise intensity, it will show a maximum at some moderate value of noise intensity.

We have already derived a map, (27)-(29), for the sinusoidally forced system (1)-(2), and we can use this to show stochastic resonance in (1)-(2), since it already incorporates a signal — the sinusoid. One choice of modeling the effect of noise is to replace (29) by

$$c_{n+1} = h(t_n, s_n, c_n) + \varepsilon\theta_n \tag{41}$$

where the θ_n are chosen from a normal distribution with mean zero and standard deviation 1. This noise could be due to the e.g. the probabilistic nature of the opening and closing of ion channels on the neuron being modeled, or the stochastic nature of synaptic transmission from presynaptic neurons. The parameter ε controls the noise intensity.

In order to quantify the signal to noise ratio, we need to choose which aspect of the system (1)-(2) is to be considered as the output. As was done in [23], we use the high–frequency "doublets" that occur at the end of a burst. These could be detected preferentially by, for example, a synapse with facilitation that acts over a doublet ISI, but not over a typical ISI involved in periodic firing. High frequency doublets have been linked to synchronization and communication over long distances in the brain [8, 36]. It has also been suggested that bursts (whose presence would be signaled by a doublet, in this example) rather than spikes may be the important unit of information in neural communication [25].

Thus for a set of N iterates of (27), (28) and (41) we define the output signal to be

$$f(t) = \sum_j \delta(t - \nu_j) \tag{42}$$

where

$$\{\nu_j\} = \{t_i : t_i - t_{i-1} < \rho\}_{i=2}^{N} \tag{43}$$

so $f(t)$ consists of a sum of delta functions at the times of the second spike in a pair whose ISI is less than ρ. Passing $f(t)$ through a Hanning window [30] defined over the interval $[t_1, t_N]$ and taking the Fourier transform we have

$$F(\omega) = \frac{1}{2}\sum_j e^{i\omega\nu_j}\left[1 - \cos\left(\frac{2\pi\nu_j}{t_N - t_1}\right)\right] \tag{44}$$

and the power spectrum is $|F(\omega)|^2$. An example is shown in Figure 12 for $\rho = 0.6$ and $N = 3000$ (the results of 5 realizations have been averaged). A clear increase in power at the driving frequency ($\omega = 0.1$) is seen as ε increases, but if it is increased too far, more power appears at nearby frequencies. This is quantified in Figure 13, where we have plotted the ratio of the power at the driving frequency (0.1) to the average of the power in the range $(0.07, 0.09) \bigcup (0.11, 0.13)$. This signal to noise ratio clearly increases and then decreases as the noise intensity, ε, increases, a characteristic of stochastic resonance. This behavior is also seen if the full system, (1)-(2), is simulated with Gaussian white noise added to either the dynamics of V, or the dynamics of c (not shown).

4 Summary and discussion

We have presented and analyzed a two–variable delay–differential equation model for a pyramidal cell in the electrosensory lateral line lobe of a weakly electric fish. We have concentrated on the "bursting" behavior seen in these cells. The model was a simplification of the six variable ODE model presented in [5], which was itself a drastic simplification of the multicompartment model of [6]. The simplicity of our model has allowed us to derive a two–variable map for firing times of the model neuron, and to determine how the model's behavior depends on its parameters. To our knowledge, this is the first reduction of a bursting system to an analytical map. The modeling of backpropagation in active dendrites by a delay is also novel, and may be useful in modeling other systems in which current flow between parts of a cell are important [9, 16, 20, 26, 28, 33].

We have also considered the effects of sinusoidal forcing on the model neuron, and have derived a three–variable map for firing times. This map has allowed us to analytically determine the boundaries of phase–locked regions (Arnold tongues) and, by adding noise to the three–variable map, to demonstrate stochastic resonance in the model.

Other similar work includes [4], which involves the analysis of periodic forcing of an integrate–and–fire–or–burst model neuron. The model was first presented in [34] and, like ours, is piecewise linear. It consists of a standard integrate–and–fire model with the addition of a second variable meant to represent inactivation of a low–threshold Ca^{2+} conductance. The inclusion of this extra variable means that the model is capable of postinhibitory rebound bursting. Rulkov [32] recently introduced a two–variable map that produced square–wave bursting, but for that map, iterates sweep out "spikes", and do not correspond to spike times. Also, it was not derived from a continuous–time system. And Goldbeter [13] has discussed piecewise linear maps that show bursting behavior — these are approximations to Poincare maps derived from continuous–time systems. None of these models involved soma–dendrite interactions, so our model is novel in that respect.

A simple model such as the one presented here is amenable to interesting extensions. One example would be to make the refractory period of the dendrite, r, a dynamic variable, so that it increased during a burst. Then a burst could be terminated by a decreasing ISI meeting an increasing refractory period, resulting in the failure to produce a DAP. Another example could involve including a refractory period in the soma and investigating the effects of changing the relative refractory periods in the two compartments. Even if analytical expressions could not be obtained under these modifications, the computational simplicity of the model presented here would enable one to gain insight into their effects.

More generally, it may be possible to construct similar "reduced" models of other types of bursting cells [17]. The key ingredient in the creation of (1)-(2), or similar models mentioned in the Appendix, is an understanding of the mechanisms involved in bursting.

A Other Models

The system (1)-(2) is not unique in reproducing the qualitative features of ghostbursting. Since we understand the mechanism involved, we can create equally valid models, each of which has its own advantages and disadvantages.

One equation that could replace (1) is

$$\frac{dV}{dt} = I - V + Ac\sum_n H(t_n - t_{n-1} - r)H(t - t_n - \sigma)e^{-\mu(t-t_n-\sigma)} \tag{45}$$

Here we have replaced the delayed delta function in (1), $\delta(t - t_n - \sigma)$, by a decaying exponential that is zero before $t - t_n - \sigma$, namely $H(t - t_n - \sigma)e^{-\mu(t-t_n-\sigma)}$. For this form of delayed feedback, V would be continuous at $t - t_n - \sigma$, although its first derivative would not (V would still be discontinuous at firing times). Another alternative to (1) is

$$\frac{dV}{dt} = I - V + Ac\sum_n H(t_n - t_{n-1} - r)s(t - t_n) \tag{46}$$

where

$$s(t) = \frac{ab}{b-a}H(t)(e^{-at} - e^{-bt}), \qquad 0 < a < b \tag{47}$$

and the contribution to the term involving s from firings other than the most recent may or may not be taken into account. For (46)-(47), V and its first derivative will be continuous between firings, and the time to the peak of s can be related to the effective delay between a somatic action potential and the maximum flow of current from dendrite to soma. A disadvantage of using these smoother forms of delayed feedback is that even in the unforced case, the map (7)-(8) can no longer be written explicitly, but will involve equations that must be solved numerically.

It is also possible to replace the Heaviside function, $H(x)$, that determines whether there is effective feedback from the dendrite to soma in (1) with a smooth approximation, e.g. $[1 + \tanh(\nu x)]/2$, where ν is sufficiently large. Doing this would remove the distinction between cases (*ii*) and (*iii*) in (7). The $B + Cc^2$ term in (2) could also be replaced by an increasing function of c, but this would affect both the analytical tractability of the system and its chaotic nature.

It is also possible to have partial failure of backpropagation, rather than complete. This would involve replacing the Heaviside function in (1) with, for example

$$(1-\alpha)H(t_n - t_{n-1} - r) + \alpha H(r + t_{n-1} - t_n) \tag{48}$$

where α is a parameter. When $\alpha = 0$, we recover (1), but for small α there is still some residual effect of the last dendritic action potential in a burst. This may be more realistic, since the last dendritic action potential does not actually fail completely (see Figure 1, middle panel). This modification would also decrease the "gap" between the lowest instantaneous frequency during bursting and the next lowest (see Figure 3 and point 2 in Section 2.1).

We could also use the "theta neuron" [15] to produce action potentials, rather than the integrate–and–fire mechanism, replacing (1) with, for example,

$$\frac{d\theta}{dt} = 1 - \cos\theta + (1 + \cos\theta)[I + AcH(t_n - t_{n-1} - r)\delta(t - t_n - \sigma)] \tag{49}$$

where $\theta \in [0, 2\pi)$ and the $\{t_n\}$ are the times at which θ passes through π. For this model, the transition from quiescence to periodic firing occurs as I is increased through zero. Because the bifurcation from quiescence to periodic firing when $A = 0$ is a saddle–node–on–a–circle bifurcation, as it is in [5], this model would have the correct scaling for interburst intervals as I is decreased.

Acknowledgements: We thank Maurice Chacron and Brent Doiron for helpful conversations regarding the ideas presented here. This work was funded by NSERC and a PREA award from the government of Ontario.

References

[1] Chacron, M. J., A. Longtin and L. Maler (2001). Negative interspike interval correlations increase the neuronal capacity for encoding time–dependent stimuli. *J. Neurosci.* **21**(14), 5328-5343.

[2] Chacron, M. J., K. Pakdaman and A. Longtin (2001). Interspike interval correlations, phase–locking , and chaotic dynamics in a leaky integrate–and–fire model with dynamic threshold. Submitted.

[3] Coombes, S. and P. C. Bressloff (1999). Mode locking and Arnold tongues in integrate–and–fire neural oscillators. *Phys. Rev. E* **60**(2), 2086-2096.

[4] Coombes, S., M. R. Owen and G. D. Smith (2001). Mode locking in a periodically forced integrate–and–fire–or–burst neuron model. *Phys. Rev. E* **64**(4), 041914.

[5] Doiron, B., C. R. Laing, A. Longtin and L. Maler (2001). "Ghostbursting": a novel bursting mechanism in pyramidal cells. To appear in *J. Comput. Neurosci.*

[6] Doiron, B., A. Longtin, R. W. Turner and L. Maler (2001). Model of gamma frequency burst discharge generated by conditional backpropagation. *J. Neurophysiol.* **86** 1523-1545.

[7] Doiron, B., L. Noonan, R. W. Turner, A. Longtin and L. Maler (2001). Shifting burst threshold with dendritic conductances. XXXI Proc. Soc. Neurosci., San Diego.

[8] Ermentrout, G. B. and N. Kopell (1998). Fine structure of neural spiking and synchronization in the presence of conduction delays. *Proc. Natl. Acad. Sci. USA* **95** 1259-1264.

[9] Ermentrout, G. B and J. Rinzel (1996). Reflected waves in an inhomogeneous excitable medium. *SIAM J. Appl. Math.* **56**(4) 1107-1128.

[10] Gammaitoni, L., P. Hänggi, P. Jung and F. Marchesoni (1998). Stochastic resonance. *Rev. Mod. Phys.* **70**(1) 223-287.

[11] Glass, L. and M. C. Mackey (1988). *From clocks to chaos: the rhythms of life.* Princeton University Press.

[12] Glass, L. (1991). Cardiac arrhythmias and circle maps — A classical problem. *Chaos* **1**(1) 13-19.

[13] Goldbeter, A. (1996). *Biochemical oscillations and cellular rhythms: the molecular bases of periodic and chaotic behaviour.* Cambridge University Press.

[14] Guevara, M. L., L. Glass and A. Shrier (1981). Phase locking, period–doubling bifurcations, and irregular dynamics in periodically stimulated cardiac cells. *Science* **214**, 1350-1353.

[15] Gutkin, B. S. and G. B. Ermentrout (1998). Dynamics of membrane excitability determine interspike interval variability: a link between spike generation mechanism and cortical spike train statistics. *Neural Comp.* **10** 1047-1065.

[16] Häusser, M., N. Spruston and G. J. Stuart (2000). Diversity and dynamics of dendritic signaling. *Science.* **290** 739-744.

[17] Izhikevich, E. M. (2000). Neural excitability, spiking, and bursting. *Int. J. Bifn. Chaos* **10** 1171-1266.

[18] Keener, J. P., F. C. Hoppensteadt and J. Rinzel (1981). Integrate–and–fire models of nerve membrane response to oscillatory input. *SIAM J. Appl. Math.* **41**(3) 503-517,

[19] Keener, J. and Sneyd, J. (1998). *Mathematical Physiology.* Interdisciplinary Applied Mathematics, Vol. 8. Springer–Verlag New York.

[20] Kepecs, A. and X.-J. Wang (2000). Analysis of complex bursting in cortical pyramidal neuron models. *Neurocomputing* **32-33** 181-187.

[21] Kuznetsov, Y. A. (1995). *Elements of Applied Bifurcation Theory.* Applied Mathematical Sciences, Vol. 112. Springer–Verlag.

[22] Laing, C. R. (2001). Burst excitability. In preparation.

[23] Laing, C. R. (2001). The response of bursting neurons to sinusoidal inputs. In preparation.

[24] Lemon, N. and R. W. Turner (2000). Conditional spike backpropagation generates burst discharge in a sensory neuron. *J. Neurophysiol.* **84** 1519-1530.

[25] Lisman, J. E. (1997). Bursts as units of neural information: making unreliable synapses reliable. *Trends Neurosci* **20** 38-43.

[26] Mainen, Z. F. and T. J. Sejnowski (1996). Influence of dendritic structure on firing pattern in model neocortical neurons. *Nature* **382** 363-366.

[27] Nelson, M. E., Z. Xu and J. R. Payne (1997). Characterization and modeling of P–type electrosensory afferent responses to amplitude modulations in a wave–type electric fish. *J. Comp. Physiol. A* **181** 532-544.

[28] Pinsky, P. F. and J. Rinzel (1994). Intrinsic and Network Rhythmogenesis in a Reduced Traub Model for CA3 Neurons. *J. Comput. Neurosci.* **1** 39-60.

[29] Pomeau, Y. and P. Manneville (1980). Intermittent transition to turbulence in dissipative dynamical systems. *Comm. Math. Phys.* **74** 189-197.

[30] Press, W. H., S. A. Teukolsky, W. T. Vetterling and B. P. Flannery (1992). *Numerical Recipes in C.* Cambridge University Press. Second Ed.

[31] Rinzel, J. and G. B. Ermentrout (1998). Analysis of neural excitability and oscillations. In *Methods in Neuronal Modeling: From Ions to Networks.* Ed. C. Koch and I. Segev. MIT Press.

[32] Rulkov, N. F. (2000). Regularization of synchronized chaotic bursts. *Phys. Rev. Lett.* **86**(1) 183-186.

[33] Segev, I. and W. Rall (1998). Excitable dendrites and spines: earlier theoretical insights elucidate recent direct observations. *Trends Neurosci.* **21** 453-460.

[34] Smith, G. D., C. L. Cox, S. M. Sherman and J. Rinzel (2000). Fourier analysis of sinusoidally driven thalamocortical relay neurons and a minimal integrate–and–fire–or–burst model. *J. Neurophysiol.* **83** 588-610.

[35] Strogatz, S. H. (1994). *Nonlinear dynamics and chaos: with applications to physics, biology, chemistry, and engineering.* Addison–Wesley. Reading.

[36] Traub, R. D., M. A. Whittington, I. M. Stanford and J. G. Jefferys (1996). A mechanism for generation of long–range synchronous fast oscillations in the cortex. *Nature* **383** 621-624.

[37] R. W. Turner, personal communication.

[38] de Vreis, G. (1998). Multiple bifurcations in a polynomial model of bursting oscillations. *J. Nonlinear Sci.* **8** 281-316.

[39] Wang, X.-J. (1993). Genesis of bursting oscillations in the Hindmarsh–Rose model and homoclinicity to a chaotic saddle. *Physica D.* **62** 263-274.

[40] Wang, X.-J. (1999). Fast burst firing and short–term synaptic plasticity: A model of neocortical chattering neurons. *Neurosci.* **89**(2) 347-362.

[41] Yoshino, K., T. Nomura, K. Pakdaman and S. Sato (1999). Synthetic analysis of periodically stimulated excitable and oscillatory membrane models. *Phys. Rev. E.* **59**(1), 956-969.

List of Figures

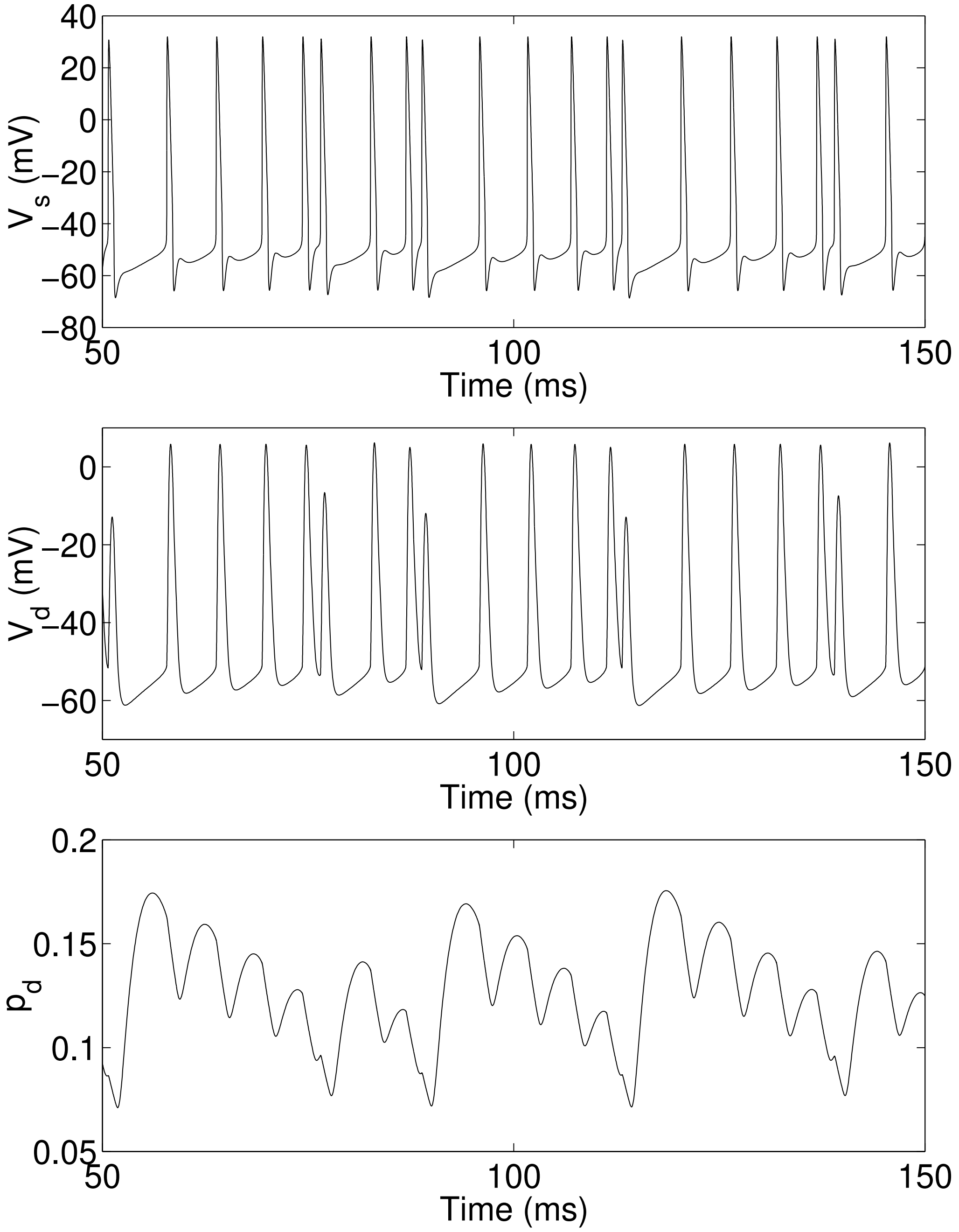

Figure 1: An example of bursting for the 6–variable ODE model of [5]. Top: somatic voltage, middle: dendritic voltage, bottom: dendritic potassium inactivation. Bursts terminate at t approximately 75, 90, 115 and 140. Note the progressively smaller ISIs during a burst, and the dendritic spike failure at the end of each burst.

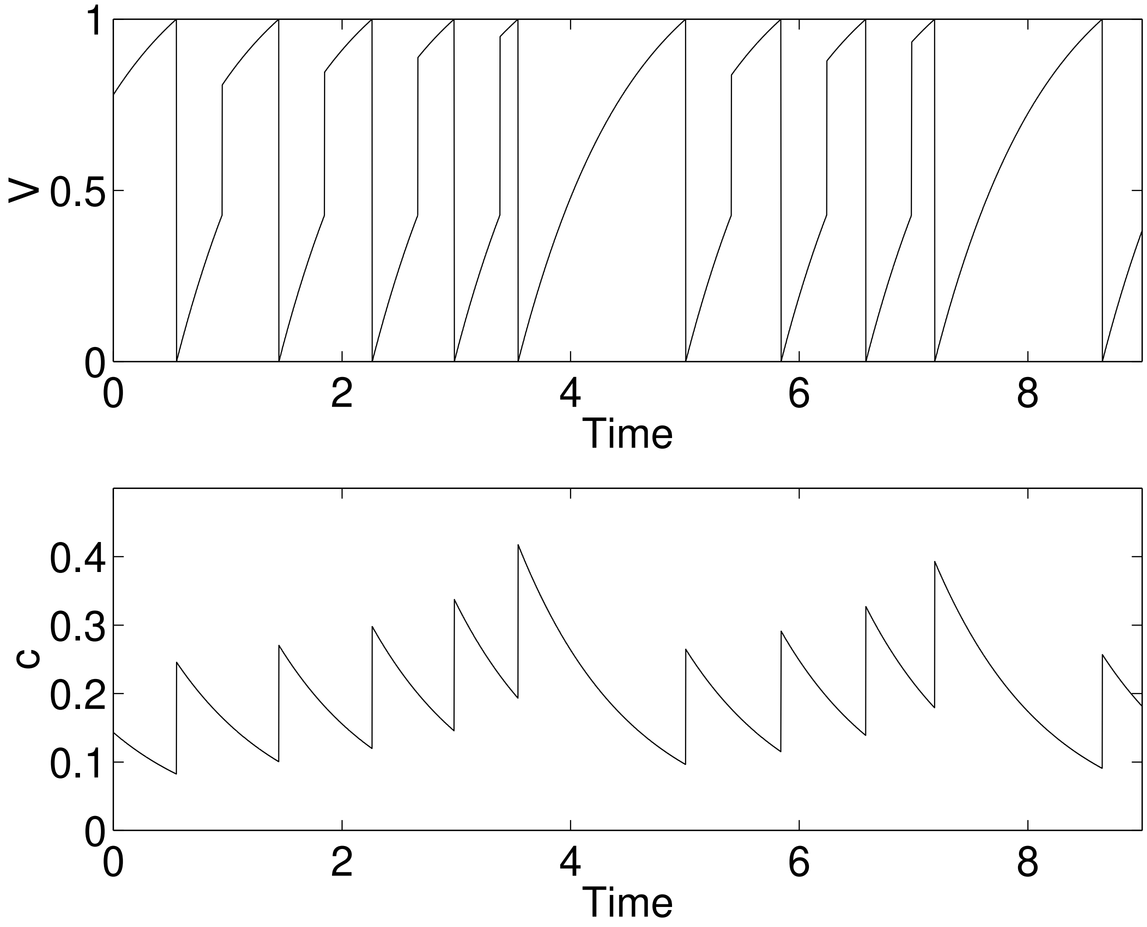

Figure 2: Voltage (top) and c, the variable representing the amount of feedback from the dendrite to the soma (bottom), as functions of time, illustrating the bursting behavior of (1)-(2). Parameters are $I = 1.3$, $A = 2.3$, $B = 0.15$, $C = 2$, $r = 0.7$, $\sigma = 0.4$, $\tau = 1$.

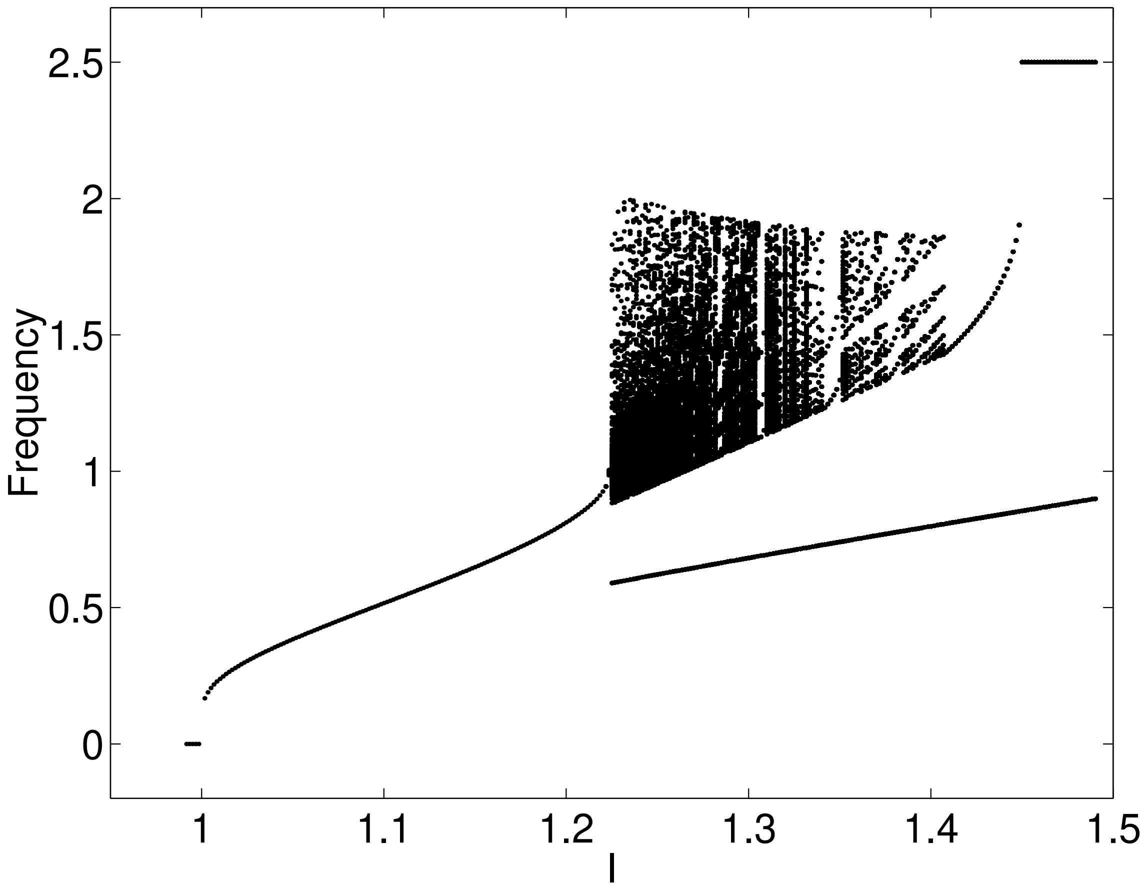

Figure 3: Instantaneous frequency (reciprocal of ISI) as a function of input current, I, for the map (7)-(8) (transients have been removed). Parameters are $A = 2.3$, $B = 0.15$, $C = 2$, $r = 0.7$, $\sigma = 0.4$, $\tau = 1$.

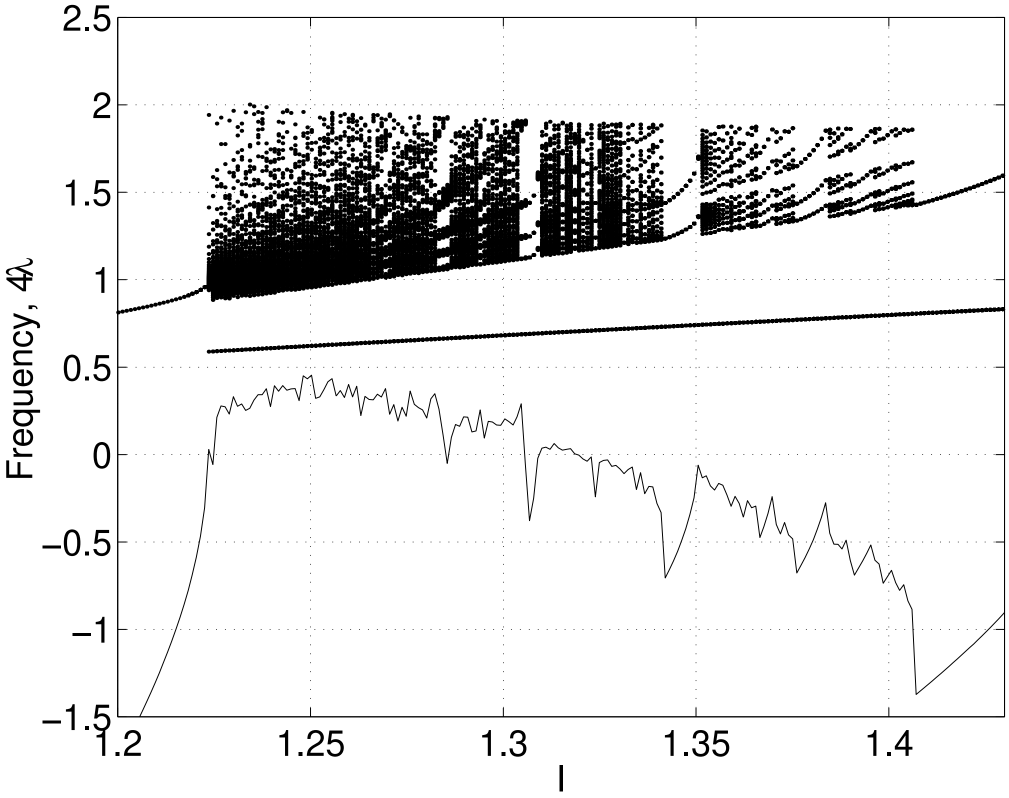

Figure 4: Instantaneous frequency and 4 times the most positive Lyapunov exponent (λ), as a function of input current, I, for the map (7)-(8). Parameters are as in Figure 3.

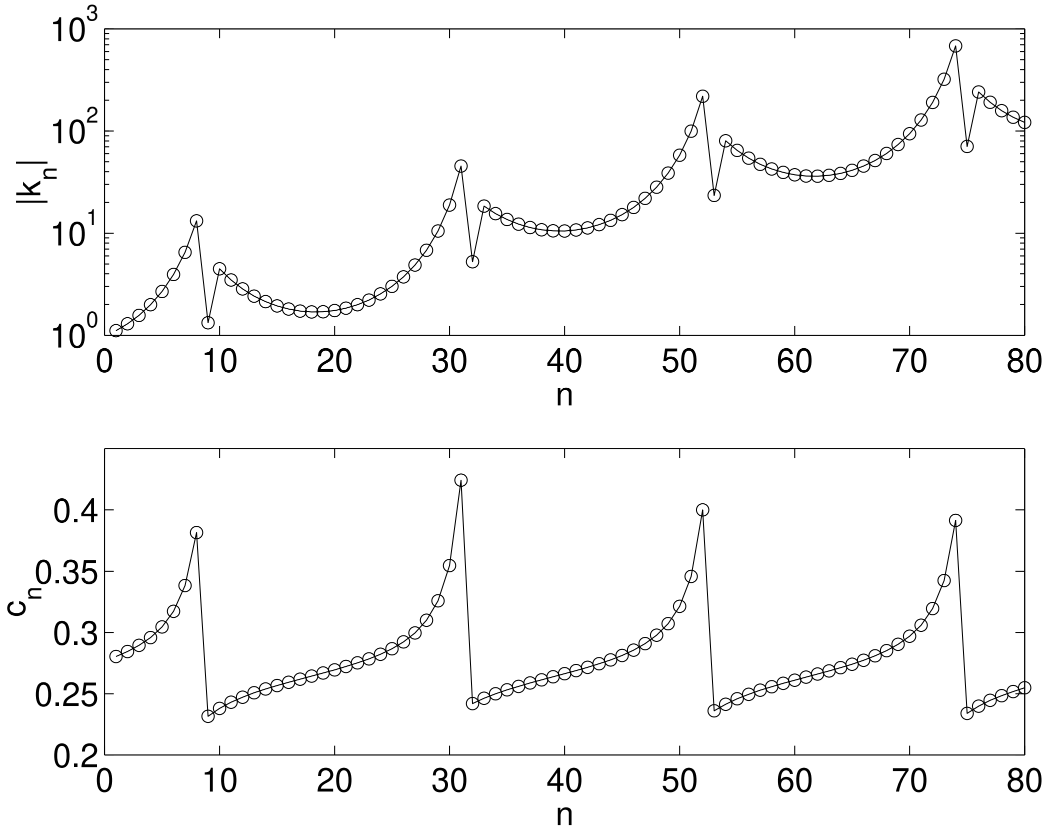

Figure 5: Top: norm of k_n, (11), as a function of n for a chaotic trajectory. Bottom: c_n as a function of n. Note that the k_n actually shrink during the first part of a burst, but grow towards the end of it. On average, the k_n grow exponentially with time, resulting in a positive Lyapunov exponent. Parameters are as in Figure 3, with $I = 1.23$.

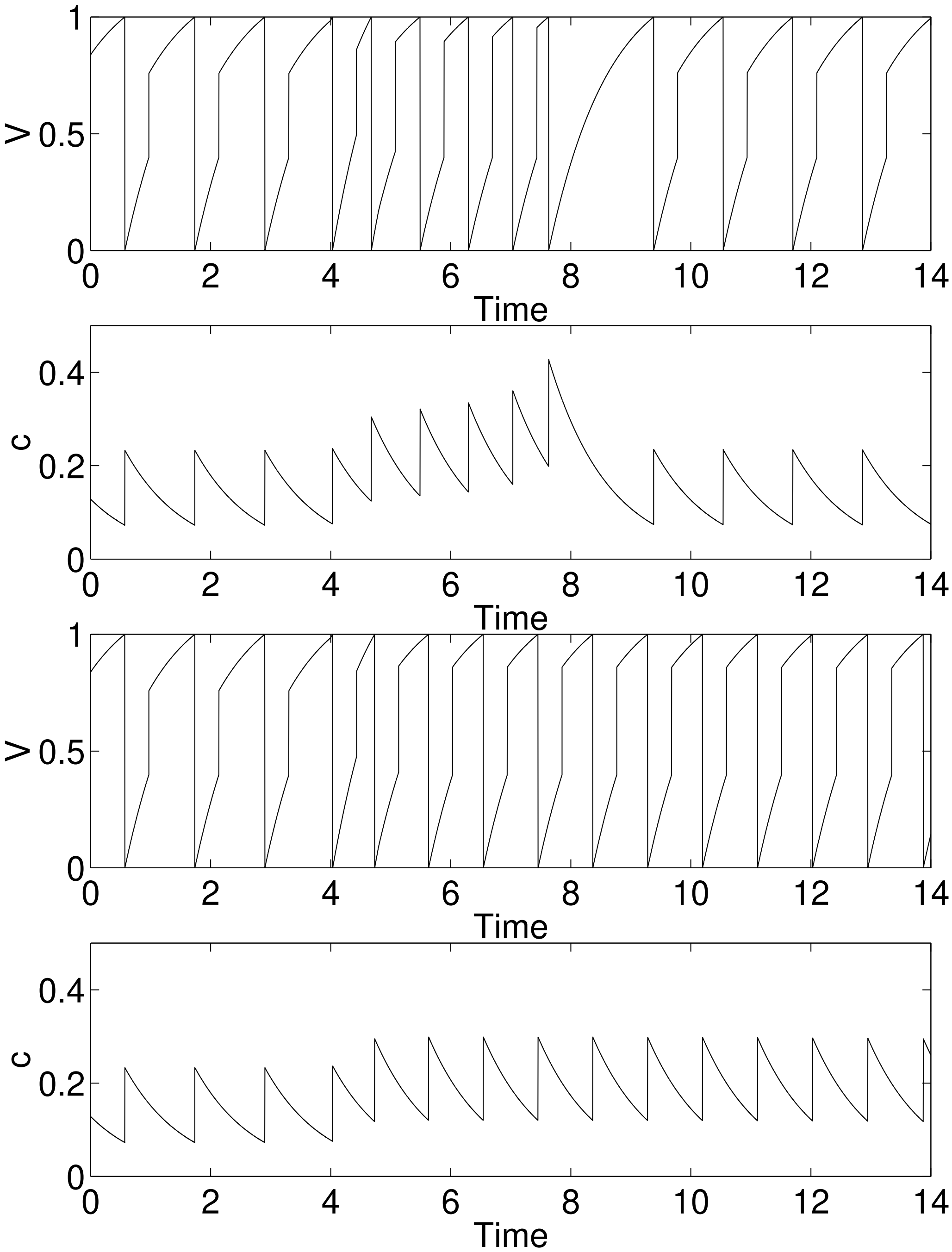

Figure 6: Burst excitability for the system (1)-(2). I was set to 1.5 for $4 < t < 4.8$ for the top two panels, and 1.45 for $4 < t < 4.8$ for the bottom two panels. $I = 1.21$ otherwise. In the top two panels a burst is induced, and in the lower two no burst is induced. Parameters are $A = 2.3$, $B = 0.15$, $C = 2$, $r = 0.6$, $\sigma = 0.4$, $\tau = 1$.

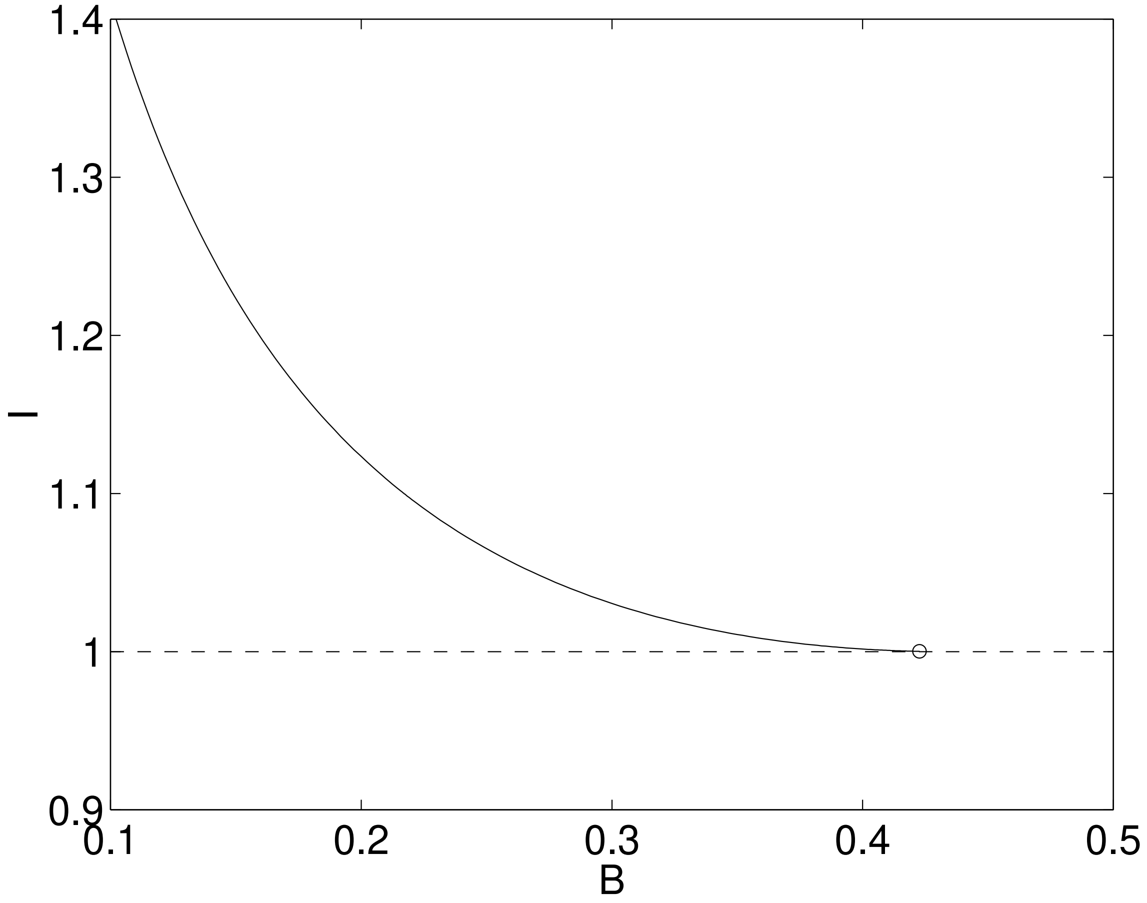

Figure 7: The curve of saddle–node bifurcations of periodic orbits (solid) and the threshold for firing (dashed), as a function of B. Other parameters are the same as in Figure 3. The two curves meet at a codimension–two point, marked with a circle.

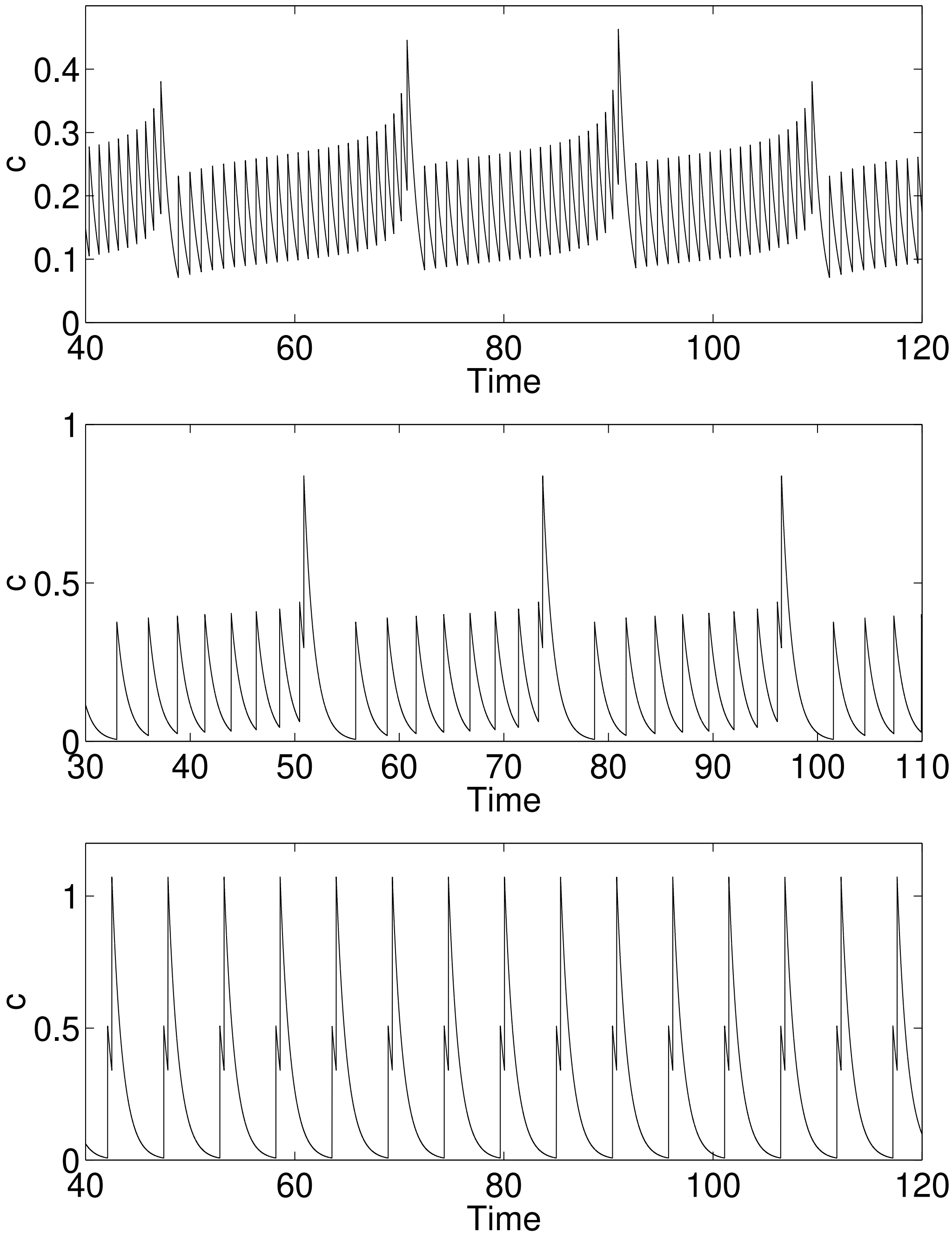

Figure 8: Example bursts of (1)-(2) for three different (I, B) pairs. Top: $(I, B) = (1.23, 0.15)$, middle: $(I, B) = (1.007, 0.37)$, bottom: $(I, B) = (1.007, 0.5)$. See Figure 7. Other parameters are the same as in Figure 3. Note that the horizontal axes all have the same scale.

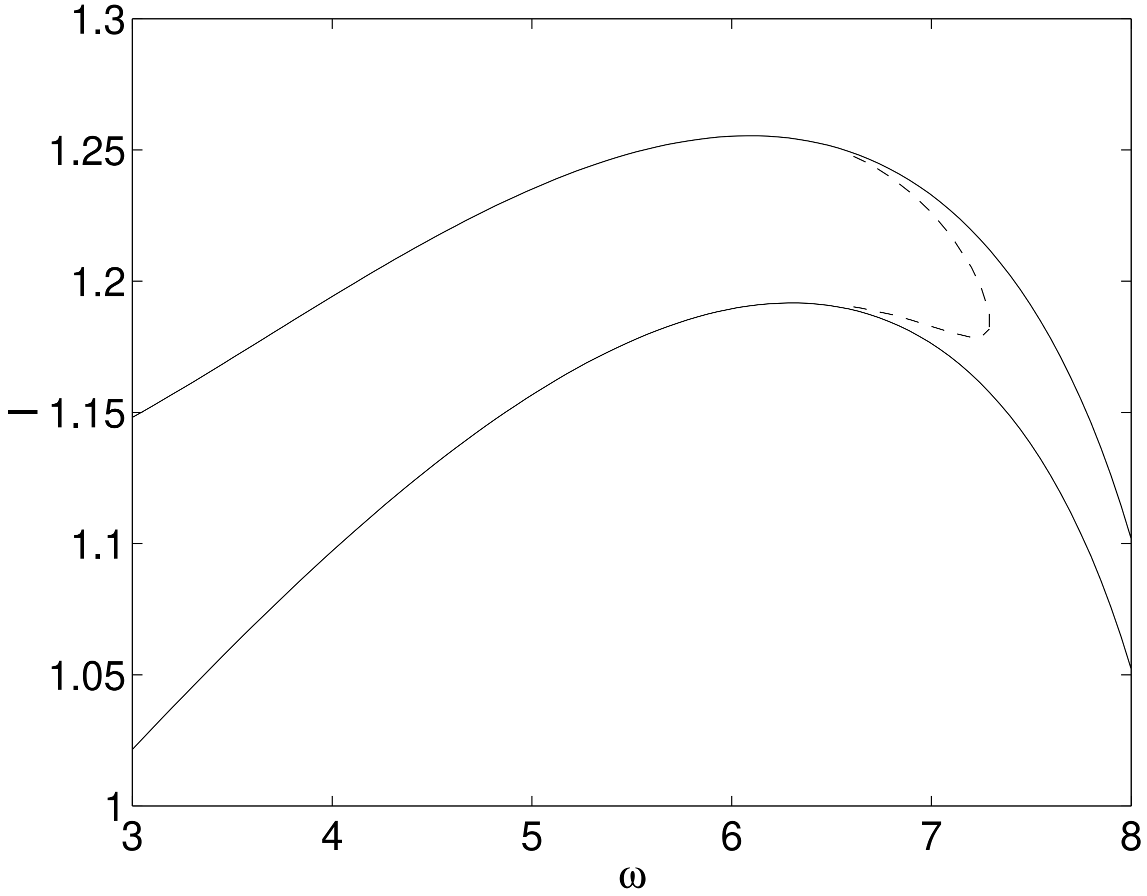

Figure 9: Boundaries of the 1 : 1 tongue from (40) (solid line) for the map (27)-(29). The dashed line indicates the curve of subcritical Hopf bifurcations. $\Gamma = 0.2$, other parameters are as in Figure 3.

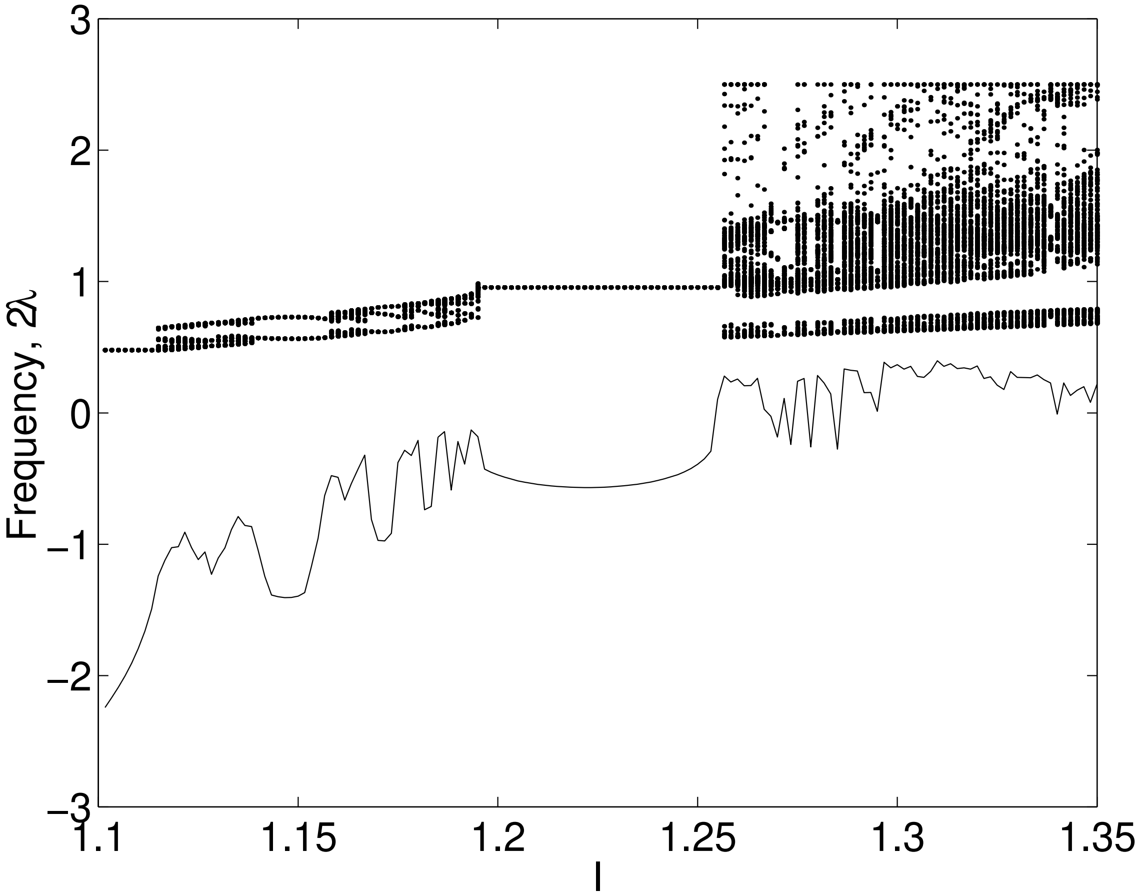

Figure 10: Instantaneous frequency (dots) and 2 times the maximal Lyapunov exponent (solid line) as a function of I for $\omega = 6$. With no periodic forcing the system shows bursts for I greater than ~ 1.22, so in this case, periodic forcing *increases* the value of I at which the periodic $\rightarrow$ bursting transition occurs. $\Gamma = 0.2$, other parameters are as in Figure 3.

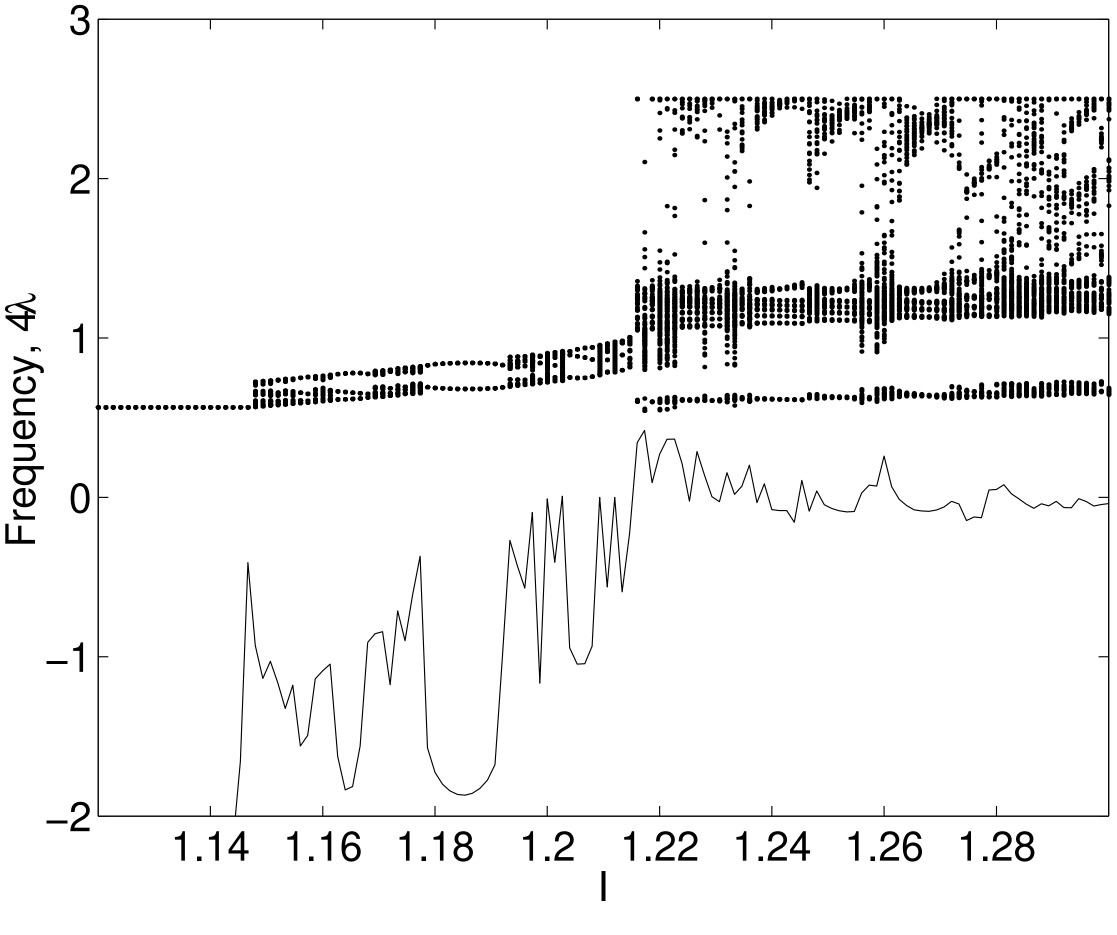

Figure 11: Instantaneous frequency (dots) and 4 times the maximal lyapunov exponent (solid line) as a function of I for $\omega = 7.1$. With no periodic forcing the system shows bursts for I greater than ~ 1.22, so in this case, periodic forcing *decreases* the value of I at which the periodic $\rightarrow$ bursting transition occurs. $\Gamma = 0.2$, other parameters are as in Figure 3.

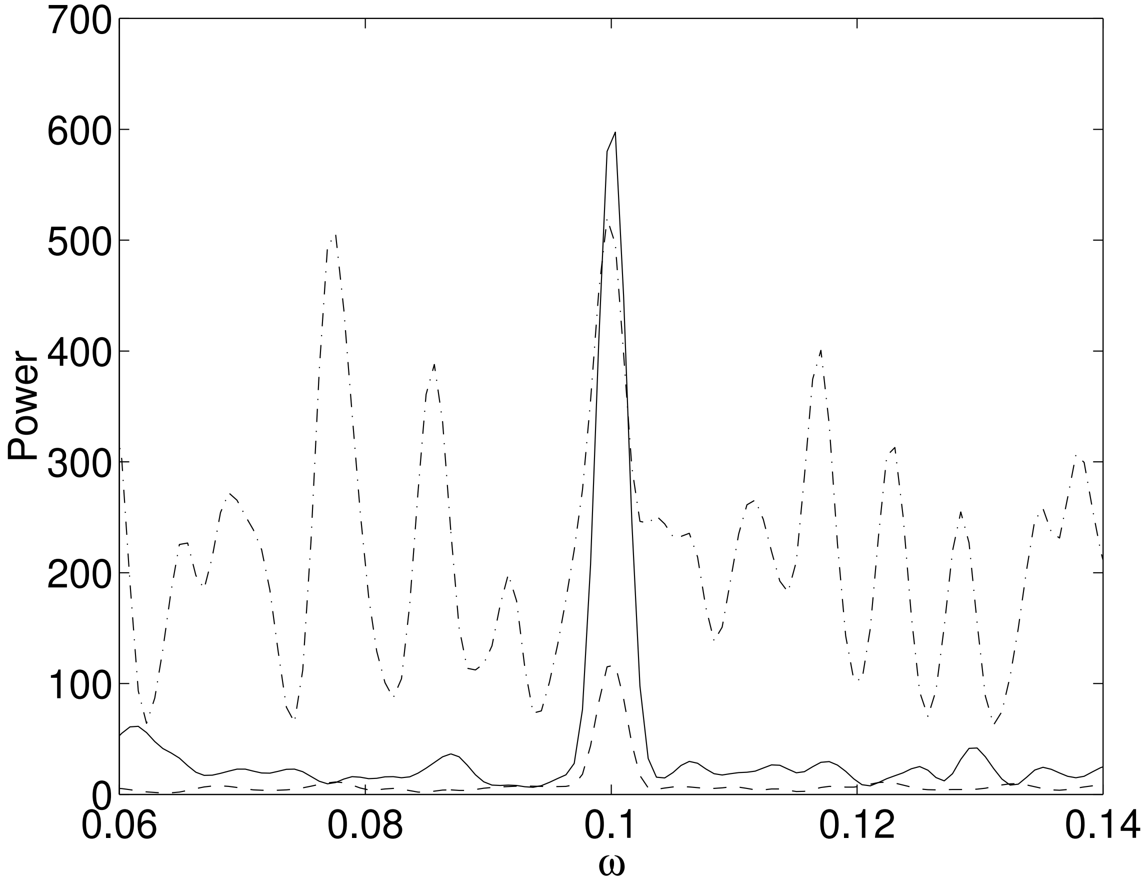

Figure 12: The power spectrum of (27), (28) and (41) as defined in (42)-(44) for $\varepsilon = e^{-6}$ (dashed), $\varepsilon = e^{-4}$ (solid) and $\varepsilon = e^{-2}$ (dash–dotted). Other parameter values are $I = 1.21$, $A = 2.3$, $B = 0.15$, $C = 2$, $\sigma = 0.4$, $\tau = 1$, $r = 0.6$, $\Gamma = 0.02$, $\omega = 0.1$. The spectra result from averaging over 5 noise realizations with $N = 3000$. Note that $I = 1.21$ is just below the bifurcation separating periodic from burst firing (see Figure 3).

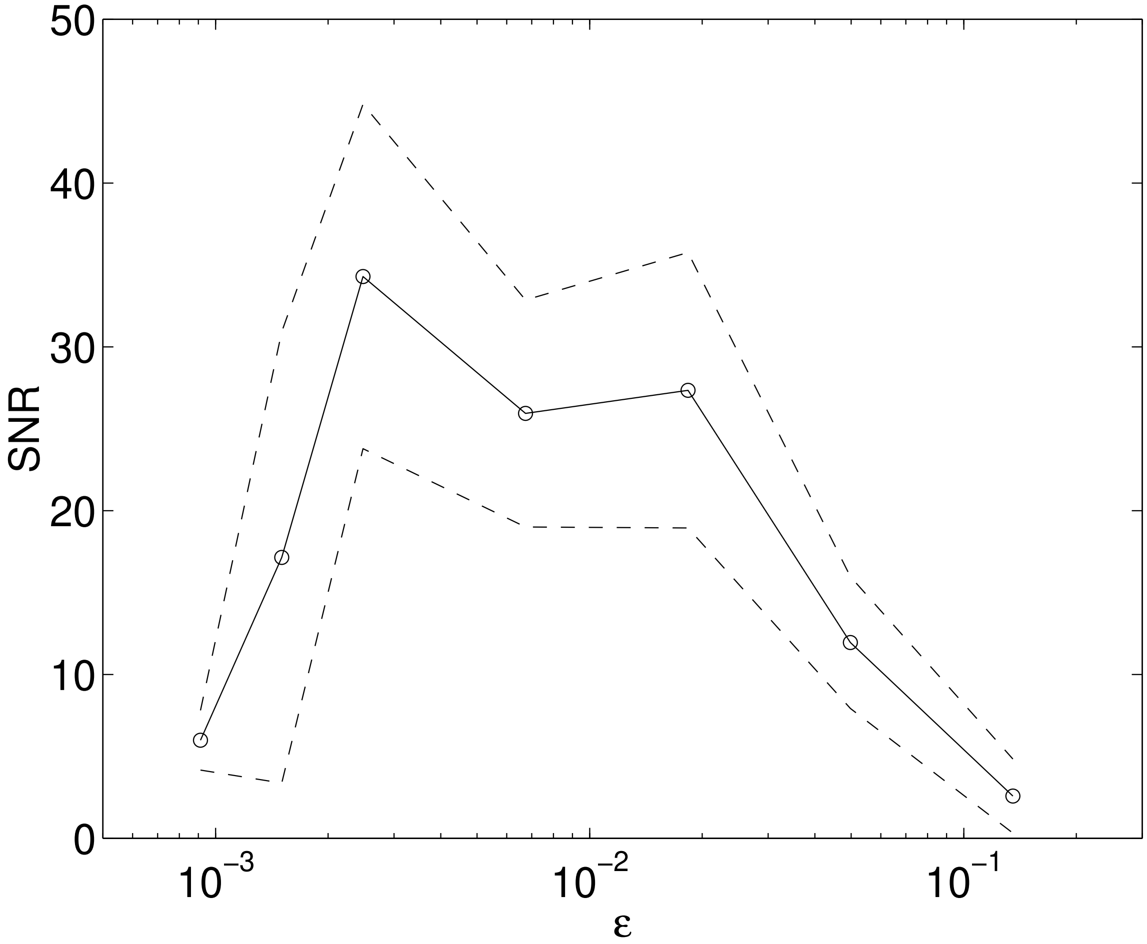

Figure 13: The signal to noise ratio of (27), (28) and (41) as defined in (42)-(44) as a function of ε. Parameters are as in Figure 12. The dashed lines indicate $\pm$ one standard deviation.